1   **On the origin of the marine zinc–silicon correlation**

2

3   Gregory F. de Souza[a,*], Samar P. Khatiwala[b], Mathis P. Hain[c], Susan H. Little[d] and Derek Vance[a]

4

5   [a] ETH Zurich, Institute of Geochemistry and Petrology, Clausiusstrasse 25, 8092 Zurich, Switzerland

6   [b] Department of Earth Sciences, University of Oxford, South Parks Road, Oxford OX1 3AN, UK

7   [c] National Oceanography Centre, University of Southampton, Southampton SO14 3ZH, UK

8   [d] Department of Earth Science and Engineering, Imperial College London, London SW7 2BP, UK

9

10   * to whom correspondence should be addressed: ETH Zurich, Institute of Geochemistry and

11   Petrology, NW C83.1, Clausiusstrasse 25, 8092 Zurich, Switzerland; Tel: +41 44 632 6983; E-mail:

12   desouza@erdw.ethz.ch

13

14

17

19   **Abstract**

20   The close linear correlation between the distributions of dissolved zinc (Zn) and silicon (Si) in seawater

21   has puzzled chemical oceanographers since its discovery almost forty years ago, due to the apparent

22   lack of a mechanism for coupling these two nutrient elements. Recent research has shown that such a

23   correlation can be produced in an ocean model without any explicit coupling between Zn and Si, via the

24   export of Zn-rich biogenic particles in the Southern Ocean, consistent with the observation of elevated

25   Zn quotas in Southern Ocean diatoms. Here, we investigate the physical and biological mechanisms by

26   which Southern Ocean uptake and export control the large-scale marine Zn distribution, using suites of

27   sensitivity simulations in an ocean general circulation model (OGCM) and a box-model ensemble.

28   These simulations focus on the sensitivity of the Zn distribution to the stoichiometry of Zn uptake

29   relative to phosphate (PO_4), drawing directly on observations in culture. Our analysis reveals that

30   OGCM model variants that produce a well-defined step between relatively constant, high $Zn:PO_4$ uptake

31   ratios in the Southern Ocean and low $Zn:PO_4$ ratios at lower latitudes fare best in reproducing the marine

32   Zn–Si correlation at both the global and the regional Southern Ocean scale, suggesting the presence of

33   distinct Zn-biogeochemical regimes in the high- and low-latitude oceans that may relate to differences

34   in physiology, ecology or (micro-)nutrient status. Furthermore, a study of the systematics of both the

35   box model and the OGCM reveals that regional Southern Ocean Zn uptake exerts control over the global

36   Zn distribution via its modulation of the biogeochemical characteristics of the surface Southern Ocean.

37   Specifically, model variants with elevated Southern Ocean $Zn:PO_4$ uptake ratios produce near-complete

38   Zn depletion in the Si-poor surface Subantarctic Zone, where upper-ocean water masses with key roles

39   in the global oceanic circulation are formed. By setting the main preformed covariation trend within the

40   ocean interior, the subduction of these Zn- and Si-poor water masses produces a close correlation

41   between the Zn and Si distributions that is barely altered by their differential remineralisation during

42   low-latitude cycling. We speculate that analogous processes in the high-latitude oceans may operate for

43   other trace metal micronutrients as well, splitting the ocean into two fundamentally different

44   biogeochemical, and thus biogeographic, regimes.

1. Introduction

As a phytoplankton micronutrient, zinc is a highly versatile element, playing a role as co-factor in metalloenzymes required for biological tasks as varied as carbon fixation (Price and Badger, 1989), gene expression (Twining and Baines, 2013) and the uptake of key macronutrients such as phosphorus and, potentially, silicon (Rueter and Morel, 1981; Sherbakova et al., 2005; Morel et al., 2014). Indeed, the physiological importance of zinc rivals that of iron (Fe), with more Zn-bearing metalloenzymes known than Fe-bearing ones (Morel et al., 2014). And yet the marine Zn cycle has received limited attention, most likely the result of a long-standing lack of observational data on the abundance of dissolved Zn in the sea. Within the last five years, the efforts of the GEOTRACES programme have produced an order-of-magnitude change in the volume of marine Zn abundance data (Mawji et al., 2015).

In a recent companion study, Vance et al. (2017) took advantage of this step-change in data availability to study the mechanisms responsible for producing the observed oceanic Zn distribution. It has been known since the very first reliable analyses of oceanic Zn concentration (Bruland, 1980) that the Zn distribution mimics that of dissolved silicon, a macronutrient that is obligatorily required, and dominantly cycled, by the siliceous phytoplankton known as diatoms. The reasons for the very close, near-linear correlation (Fig. S3) between these two elements in the ocean has, however, remained unclear for over three decades. A direct mechanism, such as the incorporation of Zn into the siliceous frustules of diatoms (Broecker and Peng, 1982), is not permitted by the observation that the Zn content of diatom frustules is orders of magnitude too small to produce the observed correlation between Zn and Si (Ellwood and Hunter, 2000). Furthermore, recent cellular-level elemental mapping has revealed that Zn is mostly associated with the organic matter of diatoms (Twining et al., 2004), consistent with its important physiological role, and that cellular Zn is remineralised from sinking diatom detritus at shallow depths together with phosphorus, not at the greater depths at which siliceous hard parts dissolve (Twining et al., 2014). Thus, the simple correlation between the marine distributions of Zn and Si at the global scale appears at odds with their contrasting biochemical roles and marine biogeochemical behaviour.

Vance et al. (2017) resolved this apparent paradox by drawing on the observation that diatoms in the Southern Ocean have cellular Zn quotas 3–15× higher than those of low-latitude phytoplankton

73   (Twining and Baines, 2013), a finding that is complemented by the observed stripping of Zn from

74   Southern Ocean surface waters (Ellwood, 2008; Zhao et al., 2014). In analogy to the well-established

75   control on the marine Si distribution by the export of Si-rich material from the surface Southern Ocean

76   (Sarmiento et al. 2007), Vance et al. (2017) proposed that strong Zn drawdown by Southern Ocean

77   diatoms with high Zn quotas is the main control on the global Zn distribution. Their ocean general

78   circulation model (OGCM) results supported this hypothesis by reproducing the observed Zn–Si

79   correlation when Southern Ocean Zn uptake was high, even in the absence of any explicit coupling

80   between the cycles of these two elements.

81   The aim of this study is to identify the mechanisms by which this emergent large-scale Zn-Si coupling

82   comes about. Our interest lies in understanding the series of interacting biological and physical processes

83   that allows Zn uptake in the remote Southern Ocean to influence the global Zn distribution. We do this

84   within the context of ocean biogeochemical models in which the cycling of Zn is explicitly tied to that

85   of phosphorus (P), and go beyond the modelling work of Vance et al. (2017) by implementing a swathe

86   of 24 OGCM sensitivity simulations as well as a 10,000-member box-model ensemble. Together, these

87   simulations reveal that Southern Ocean Zn uptake exerts global control on the marine Zn distribution

88   via its influence on the Zn status of the Subantarctic Zone (SAZ): sustained and elevated high-latitude

89   Zn uptake leads to Zn-depletion in the Si-poor SAZ, producing a low-Zn, low-Si signal that is

90   transported globally from this region by the subduction of the upper-ocean water masses Subantarctic

91   Mode Water (SAMW) and Antarctic Intermediate Water (AAIW). The systematics of the models further

92   suggest that this coupled biological-physical mechanism may apply more generally to other

93   biologically-cycled elements in the sea.

94

95   **2. Methods**

96   **2.1. Conceptual approach**

97   We wish to assess the mechanisms by which a correlation between the marine distributions of Zn and

98   Si may come about even in the absence of any explicit coupling between them. We do this in the context

99   of ocean models, described in more detail below, that simulate the marine biogeochemical cycles of P,

4

100   Zn and Si. In formulating the biogeochemical model, we were guided by the observations and constraints

101   discussed in Section 1. Thus, our model explicitly couples the cycling of Zn to that of P, reflecting

102   observations of Zn uptake in culture, our understanding of the physiological role of Zn as a

103   micronutrient, and direct observation of the Zn distribution within phytoplankton cells (Sunda and

104   Hunstman, 1992; Twining et al., 2004; Twining and Baines, 2013). The simulated surface-ocean uptake

105   of Zn is directly tied to that of PO_4 by a stoichiometric parameter $r_{Zn:P}$, which is the key variable in our

106   sensitivity analysis (see Section 2.2). Additionally, once exported from the surface ocean by sinking

107   particles, Zn is remineralised over the same short length-scale as P, as indicated by observations of

108   sinking diatoms (Twining et al., 2014). In contrast, simulated Si uptake is entirely independent of PO_4

109   uptake, and the length-scale of opal dissolution is greater than that of Zn or P remineralisation, rendering

110   its cycling entirely biogeochemically independent.

111   **2.2. Stoichiometry of simulated Zn uptake**

112   The control parameter in our suite of sensitivity simulations is the stoichiometric parameter $r_{Zn:P}$, which

113   links the uptake of Zn to the simulated PO_4 uptake. Our parameterisation of $r_{Zn:P}$ is based on results from

114   laboratory cultures of three diatom species and two clones of the prymnesiophyte *E. huxleyi* by Sunda

115   and Huntsman (1992). They observed that the Zn:C (and, by extension, Zn:P) ratio of phytoplankton

116   uptake is a non-linear function of the Zn^{2+} concentration of the growth medium, described by an equation

117   of the form:

118   $$r_{Zn:P} = \frac{a_{Zn} \cdot Zn^{2+}}{b_{Zn} + Zn^{2+}} + c_{Zn} \cdot Zn^{2+} \qquad \text{(Eqn. 1)}$$

$$\text{(I)} \qquad\qquad \text{(II)}$$

119   This equation is the linear superposition of a saturating Michaelis-Menten term (I) and a non-saturating

120   linear term (II), which is illustrated by the shape of curves fit to the culture data of Sunda and Huntsman

121   (1992) in Fig. 1a. The species Zn^{2+} represents free aqueous Zn in solution, i.e. Zn that is neither

122   inorganically nor organically complexed. Considering only organic speciation, the concentration of Zn^{2+}

123   is governed by the total concentration of dissolved Zn on the one hand, and the concentration (and

124   binding characteristics) of the chelating organic ligand on the other. We assume a globally constant

125   ligand concentration of 1.2 nM, which allows us to circumvent the explicit simulation of Zn

126   complexation chemistry (see Supplementary Information). The assumption of constant ligand

127   concentrations is doubtless an oversimplification, but the sparse observational dataset shows only

128   limited variability (~0.6–2.4 nM) with no systematic variation (Donat and Bruland, 1990; Bruland,

129   1989; Ellwood and van den Berg, 2000; Ellwood, 2004; Lohan et al., 2005; Baars and Croot, 2011).

130   This variability in ligand concentrations is small relative to the orders-of-magnitude variability of

131   dissolved Zn in the ocean. Sensitivity simulations documented in the Supplementary Information (Fig.

132   S11) show that the choice of ligand concentration does not affect the systematics of our results, and thus

133   has no influence on our interpretation.

134   Parameters a_{Zn}, b_{Zn} and c_{Zn} of Eqn. 1 control different aspects of the dependency of $r_{Zn:P}$ on Zn^{2+}, as

135   illustrated schematically in Fig. 1b. Parameter a_{Zn} determines the maximum asymptotic $Zn:PO_4$ ratio of

136   uptake when the Michaelis-Menten term of Eqn. 1 saturates, whilst b_{Zn} controls the sensitivity of $r_{Zn:P}$

137   to low Zn^{2+} concentrations. The linear parameter c_{Zn}, on the other hand, determines the extent to which

138   high Zn^{2+} affects $r_{Zn:P}$ beyond the asymptotic $Zn:PO_4$ ratio determined by a_{Zn}. In this paper, we present

139   the results of 24 OGCM sensitivity simulations in which the values of these parameters are varied (Table

140   1). In our base suite of simulations (G1-G11), also presented in Vance et al. (2017), the values of a_{Zn},

141   b_{Zn} and c_{Zn} are set so as to reproduce the dependence of $r_{Zn:P}$ on Zn^{2+} in the culture data of Sunda and

142   Huntsman (1992), i.e. the curves shown in Fig. 1a (G7-G11), or an approximation thereof in which $r_{Zn:P}$

143   is a linear function of Zn concentration (G1-G6; see Supplementary Information). In a further 13

144   simulations (G12-G24), parameters a_{Zn}, b_{Zn} and c_{Zn} are separately varied within the bounds of the culture

145   data, in order to explore their individual influence on the spatial distribution of $r_{Zn:P}$ and the marine Zn

146   distribution.

147   **2.3. Model framework**

148   OGCM simulations were run on the high-performance cluster *Euler* at ETH Zurich using the transport-

149   matrix method (TMM) of Khatiwala et al. (2005), which allows efficient offline simulation of passive

150   tracers. Here, we use transport matrices derived from MITgcm-2.8, a coarse-resolution version of

151   MITgcm (Marshall et al., 1997) with 2.8° × 2.8° lateral resolution and 15 vertical levels (see

152   Supplementary Information). Simulations were carried out with annual-mean circulation fields derived

153   from the equilibrium state of the model, and thus do not include seasonal variability.

154   Our biogeochemical model of P, Si and Zn cycling is based on the formulation developed for the

155   OCMIP-2 project (Najjar et al., 2007), with simulated uptake of PO_4 and Si in the surface ocean driven

156   by restoring their concentrations towards observations in World Ocean Atlas 2013 (Garcia et al., 2013;

157   see Supplementary Information). As discussed in Section 2.2, Zn uptake is directly tied to that of PO_4

158   by the stoichiometric parameter $r_{Zn:P}$. Both Zn and P in the particulate export flux are remineralised

159   following a power-law depth-dependency with an exponent of -0.858 (Martin et al., 1987; Berelson,

160   2001), whereas regeneration of Si follows an exponential dependency with a length-scale of 1000 m (de

161   Souza et al., 2014). Based on World Ocean Atlas 2013 and literature data, the mean ocean concentrations

162   of PO_4, Zn and Si are set to values of 2.17 μM, 5.4 nM (Chester and Jickells, 2012) and 92 μM

163   respectively. Biogeochemical model simulations are initialised with these mean ocean concentrations

164   and integrated for 5000 model years to equilibrium.

165   In addition to the OGCM simulations, we also conducted a suite of sensitivity tests in the 18-box ocean

166   model CYCLOPS (Hain et al., 2014; after Keir, 1988) in which Zn cycling is linked to that of PO_4

167   exactly as in the OGCM. The simplicity of the box-model formulation allows us to conduct a large

168   ensemble of 10,000 simulations with varying $Zn:PO_4$ uptake behaviours. As in the OGCM suite, box-

169   model simulations are initialised with constant mean ocean concentrations of PO_4, Zn and Si as above,

170   and integrated for 5000 model years to equilibrium. Further details are in the Supplementary

171   Information.

172

173   **3. Results & Discussion**

174   We organise the analysis and discussion of our model results as follows: in Section 3.1, we review the

175   suite of 11 simulations presented by Vance et al. (2017), which represents the range of $Zn:PO_4$ uptake

176   behaviours seen in culture data (Eqn. 1; Sunda and Huntsman, 1992) and demonstrates the importance

177   of meridional variability in $Zn:PO_4$ uptake for the production of a global Zn–Si correlation. In Section

178   3.2, we implement 13 additional simulations to analyse the systematics of Southern Ocean Zn uptake in

179   detail, and show that it is Zn-depletion in the Southern Ocean's Si-poor SAZ that is necessary for our

180   model to simulate a linear Zn–Si correlation. In Section 3.3, we combine our OGCM results with a box-

181 model ensemble to illustrate the physical mechanism by which Subantarctic depletion of Zn and Si

182 causes these elements to be globally correlated, before discussing our results more broadly in Sections

183 3.4 and 3.5.

3.1. Systematics of base sensitivity simulations

185 In our base set of simulations (G1-G11) first presented by Vance et al. (2017), the parameters a_{Zn}, b_{Zn}

186 and c_{Zn} in Eqn. 1 were varied to reproduce the dependency of the Zn:PO$_4$ uptake ratio $r_{Zn:P}$ on Zn^{2+}

187 observed in the culturing experiments of Sunda and Huntsman (1992; Fig. 1). Note that these simulations

188 are not meant to represent uptake by a single type of phytoplankton; rather, the culture data are used to

189 constrain the extent to which the dependency described by Eqn. 1 may vary. Simulations G1-G11

190 produce what might be called a full spectrum of simulated Zn distributions, ranging from "PO$_4$-like" to

191 "Si-like" (i.e., closely correlated to the simulated PO$_4$ or Si distribution respectively), as illustrated by

192 the Taylor diagrams in Fig. 2a,b. In these diagrams, simulations that plot closest to the arc representing

193 a normalised standard deviation of 1 and the radial line representing a correlation coefficient of 1 (i.e.

194 the "bulls-eye" symbol in Fig. 2) show the greatest similarity between their three-dimensional Zn

195 distribution and that of Si (Fig. 2a) or PO$_4$ (Fig. 2b). Thus whilst simulation G1 produces a Zn

196 distribution that mimics that of PO$_4$, the Zn distribution of simulation G11 is highly correlated to the

197 model's distribution of Si, with a normalised standard deviation of ~1 and a correlation coefficient of

198 ~0.97 (Fig. 2a). Basin-average depth profiles (Fig. 3a-d) show the exceptional degree of similarity

199 between the Zn and Si distributions in G11, which also reproduces the observed linear Zn–Si correlation

200 in the global ocean (Fig. S3). As noted by Vance et al. (2017), these results demonstrate that given

201 specific Zn:PO$_4$ uptake formulations, a linear Zn–Si relationship can be achieved despite the difference

202 between the regeneration length-scales of Zn and Si that is built into our model. The preferential shallow

203 remineralisation of Zn manifests in the depth profiles of Fig. 3 only as a slight enrichment relative to Si

204 within the uppermost 1 km.

205 The PO$_4$ profile included for reference in Fig. 3a hints at the main control on the simulated Zn

206 distribution: since Zn and PO$_4$ are regenerated identically in our model, the marked difference between

207 their simulated distributions *must* come about due to differences in their relative uptake in the surface

208 ocean. Indeed, the observed Zn–Si correlation is best reproduced by simulations in which there is

209   significant meridional variability in the Zn:PO$_4$ uptake ratio $r_{Zn:P}$. This is shown for two contrasting

210   simulations in Fig. 4. Simulation G10 only poorly reproduces the large-scale Zn–Si correlation (Figs.

211   2a,b and S4), and simulates Southern Ocean Zn concentrations >1 nM as far north as ~40°S (Fig. 4a),

212   i.e. 10° further north than in observations (Zhao et al., 2014). In contrast, in simulation G11 (Fig. 4b),

213   which produces a Zn distribution closely correlated to that of Si (Figs. 2 and 3), surface Southern Ocean

214   Zn concentrations decrease strongly towards the north, with a sharp gradient centred around 47°S in

215   zonal average (Fig. S5a). This sharp gradient is the result of the uniformly high values of $r_{Zn:P}$ at high

216   southern latitudes, which average ~6 mmol/mol south of 47°S (Figs. 4d and S5b). Such a step-like

217   behaviour between the mid- and high-latitude oceans is in marked contrast to the gradual poleward

218   increase of $r_{Zn:P}$ in G10 (Fig. 4c), in which $r_{Zn:P}$ never exceeds 4 mmol/mol. As a result, in simulation

219   G11, Zn- and macronutrient-rich deep waters that upwell to the surface Southern Ocean in the far south

220   experience a consistently strong Zn drawdown as they are transported northwards by the simulated

221   Ekman drift, whereas in G10, $r_{Zn:P}$ is lower and decreases steadily during the northward transport of Zn-

222   rich surface waters. Analogous differences are visible in the subpolar North Atlantic and North Pacific,

223   whilst in the equatorial Pacific the opposite is true: values of $r_{Zn:P}$ are elevated in simulation G10 relative

224   to G11 (Fig. 4c,d), reflecting the unrealistically high surface Zn concentrations there (Fig. 4a).

225   Our base set of simulations thus shows that the observed correlation between the large-scale distributions

226   of Zn and Si can be reproduced even in the absence of any explicit coupling between the two elements,

227   provided that there is sufficient meridional variability in $r_{Zn:P}$. In the following, we go beyond the

228   analysis of Vance et al. (2017) and identify the mechanisms through which this surface uptake influences

229   the global Zn distribution, considering biological and physical controls in Sections 3.2 and 3.3

230   respectively.

231   **3.2. The role of biological uptake: spatial variability of $r_{Zn:P}$**

232   We take a systematic look at the effect of $r_{Zn:P}$ variability on the global Zn distribution using a suite of

233   13 sensitivity experiments in which the values of the parameters a_{Zn}, b_{Zn} and c_{Zn} in Eqn. 1 are individually

234   varied within the bounds of the observational constraints (Sunda and Hunstman, 1992; Table 1). A first

235   suite of 9 simulations (G12-G20) revealed that the Zn distribution is most sensitive to the parameters

236   a_{Zn} and c_{Zn}, whilst its sensitivity to b_{Zn} is minor (Fig. S6). In the following, we thus focus on the

237   systematics of four sensitivity simulations (G21-G24) in which permutations of the maximum and

238   minimum values of a_{Zn} and c_{Zn} are applied, whilst b_{Zn} remains constant at a mid-range value: for clarity,

239   we refer to these simulations as *aLO-cLO*, *aLO-cHI*, *aHI-cLO*, and *aHI-cHI* (Table 1). Figure 2c,d

240   demonstrates that these four simulations span the entire range of Zn–Si relationships seen in the base

241   set of simulations. Low values of both a_{Zn} and c_{Zn} (*aLO-cLO*) produce poor similarity between the Zn

242   and Si distributions (Fig. 2c). Increasing the value of c_{Zn} (*aLO-cHI*) improves the similarity of the Zn

243   and Si fields, and increasing the value of both parameters leads to yet greater similarity (*aHI-cHI*).

244   Interestingly, however, when a_{Zn} is high, reducing c_{Zn} to its minimum value results in barely any decrease

245   in the similarity between global Zn and Si fields (*aHI-cLO)*. Thus, a high value of a_{Zn} alone is sufficient

246   to produce a close similarity between the Zn and Si distributions, but a high value of c_{Zn} is not. In the

247   following, we explore the role of parameter a_{Zn} in more detail by investigating its influence on the spatial

248   distribution of the Zn:PO4 uptake ratio $r_{Zn:P}$.

249   Surface maps of $r_{Zn:P}$ (Fig. 5) reveal that when values of both a_{Zn} and c_{Zn} are low, $r_{Zn:P}$ barely shows any

250   spatial variability (Fig. 5a). Since Zn is also regenerated identically to PO4 in our model, it follows that

251   the large-scale Zn distribution in *aLO-cLO* is rather similar to the PO4 distribution (Fig. 2d). In contrast,

252   a high value of one or both of these parameters leads to a pronounced meridional gradient in $r_{Zn:P}$ (Fig.

253   5b-d), with $r_{Zn:P}$ values far exceeding the mean-ocean Zn:PO4 ratio of ~2.5 mmol/mol in the Southern

254   Ocean and other polar regions. However, the meridional gradients that result from high values of a_{Zn} or

255   c_{Zn} differ considerably: a high value of c_{Zn} produces a gradual poleward increase in $r_{Zn:P}$ (Fig. 5b), whilst

256   a high a_{Zn}-value leads to a sharply-defined step towards the poles, e.g. around 40°S in the Southern

257   Ocean (Fig. 5c). The sensitivity of $r_{Zn:P}$ to a high a_{Zn}-value is seen most clearly in the SAZ of the Pacific

258   Ocean (white stippling in Fig. 5c), where a high a_{Zn}-value elevates $r_{Zn:P}$ relative to simulations with low

259   values of a_{Zn} (Fig. 5a,b). The reason for the different responses of $r_{Zn:P}$ to changes in a_{Zn} and c_{Zn} becomes

260   clear if we recall Eqn. 1 and the effects of parameter changes on the shape of the function (Fig. 1b): a_{Zn}

261   controls the maximum value of $r_{Zn:P}$ in the non-linear, saturating Michaelis-Menten term, whilst c_{Zn}

262   represents the non-saturating, linear increase of $r_{Zn:P}$ with Zn^{2+}. A high a_{Zn}-value thus produces a strong

263   sensitivity of $r_{Zn:P}$ to even small amounts of Zn^{2+}. This sensitivity produces a sharp poleward shift to

264   high and relatively constant $r_{Zn:P}$ in high-latitude regions, where upwelling of Zn-rich waters leads to

265 elevated Zn^{2+} in the surface. The linear influence of a high c_{Zn}-value, on the other hand, produces a

266 steady poleward gradient of $r_{Zn:P}$, such that $r_{Zn:P}$ varies *within* high-latitude regions, and especially in the

267 Southern Ocean (Fig. 5b,d).

268 The consequences of the resulting differences in the Zn stoichiometry of uptake are clearly seen in the

269 surface distribution of Zn, shown as zonal averages in Fig. 6. If we compare the Zn distributions

270 produced by simulations *aLO-cLO* and *aHI-cLO*, it becomes clear that in the Southern Ocean, the main

271 consequence of an elevated a_{Zn} value is a strong southward shift of the latitude at which surface Zn is

272 nearly completely consumed. This southward shift is due to the non-linear effect of a_{Zn} discussed above,

273 which produces high $r_{Zn:P}$ even at low Zn^{2+} concentrations, such that Zn continues to be strongly drawn

274 down as Southern Ocean surface waters are transported northwards, even when they become

275 significantly depleted in Zn and Zn^{2+}. As a result, Zn concentrations south of 40°S are reduced by over

276 1nM in *aHI-cLO* relative to *aLO-cLO*, producing a surface Zn distribution that more closely matches

277 the surface Si distribution than that of PO_4. Thus in simulation *aHI-cLO*, the Southern Ocean's SAZ

278 (centred around 45°S) is strongly Zn-depleted, consistent with observations (Zhao et al., 2014).

279 Our sensitivity simulations thus demonstrate that (a) high values of the parameter a_{Zn} play the most

280 important role in producing a close similarity between the large-scale Zn and Si distributions simulated

281 by our OGCM, and that (b) the dominant surface-ocean effect of high a_{Zn}-values is to alter the surface

282 Zn distribution in the Southern Ocean, particularly by reducing Zn concentrations in the SAZ. Taken

283 together, these observations suggest a link between Subantarctic Zn depletion and the linear Zn-Si

284 relationship in the global ocean. Below, we take advantage of the computational efficiency of the 18-

285 box model CYCLOPS (Hain et al., 2014) to test this hypothesis.

286 **3.3. Linking regional uptake to global distributions via the circulation**

287 In a large ensemble of 10,000 CYCLOPS simulations, the maximum $Zn:PO_4$ uptake ratio $r_{Zn:P}$ in each

288 of the model's 8 surface ocean boxes was allowed to vary, randomly and independently, between 0 and

289 7 mmol/mol. This ensemble reveals a systematic response of the model's SAZ to changes in $Zn:PO_4$

290 uptake stoichiometry in the Southern Ocean.

291   As in the real ocean, the SAZ in CYCLOPS is fed from the south by the northward transport of surface

292   waters from the Antarctic Zone, where deep-water upwelling occurs; and it is from the SAZ that the

293   model's upper ocean boxes are ventilated (Fig. S1). The response of the SAZ to changes in $r_{Zn:P}$ is best

294   illustrated by its Zn:Si ratio, which reflects the degree of similarity between the behaviour of Zn and Si.

295   The Zn:Si ratio of the SAZ reacts strongly to changes in $r_{Zn:P}$ in the Antarctic and Subantarctic surface:

296   when Zn uptake is muted by low $r_{Zn:P}$, the Zn:Si ratio of waters upwelled to the surface Southern Ocean

297   rises as they are transported northward into the SAZ, since Si is consumed more rapidly than Zn (Fig.

298   7a). When $r_{Zn:P}$ is high, however, the Zn uptake keeps pace with the strong stripping out of Si, preventing

299   the Zn:Si ratio of surface waters from rising, and leading to a SAZ that is both Zn- and Si-depleted. As

300   a result, at $r_{Zn:P}$ values around 5.5 mmol/mol, the congruent depletion of Zn and Si produces a

301   Subantarctic Zn:Si ratio very similar to the mean-ocean value of ~0.06 mmol/mol (Fig. 7a). These

302   simulations with high Southern Ocean $r_{Zn:P}$ also exhibit the closest linear correlation between the

303   simulated global-ocean distributions of Zn and Si, reflected by correlation coefficients close to unity in

304   Fig. 7c. The box-model ensemble thus best reproduces the observed linear Zn-Si correlation when SAZ

305   Zn:Si ratios are close to the global-ocean mean (Fig. 7e).

306   The intuition gained from the box-model systematics can be directly applied to our OGCM simulations.

307   The right-hand panels of Fig. 7 show results for simulations G1−11 and G21−24 analogous to those

308   presented for the box model. From Fig. 7b, it is clear that here too, an increase of Southern Ocean $r_{Zn:P}$

309   leads to a strong decrease in the Zn:Si ratio of the SAZ. Simulations with low Southern Ocean $r_{Zn:P}$

310   produce a Subantarctic surface highly enriched in Zn relative to Si, and fare worst in reproducing the

311   global Zn–Si correlation (Fig. 7d). Conversely, simulations in which high Southern Ocean $r_{Zn:P}$ leads to

312   a Subantarctic Zn:Si ratio close to the mean-ocean value produce the best match between the global Zn

313   and Si fields (Fig. 7f).

314   The systematics of the box-model ensemble and OGCM thus strongly support the hypothesis that

315   Southern Ocean Zn uptake exerts its control on the global Zn-Si relationship via its influence on

316   Subantarctic Zn status: Figs. 7e-f make it clear that high degrees of correlation between the global Zn

317   and Si fields correspond to SAZ Zn:Si ratios close to the mean-ocean value. Given that a linear Zn-Si

318 relationship implies a constant Zn:Si ratio in the interior ocean, this correspondence suggests that the

319 SAZ is important for the global correlation since it determines the preformed Zn:Si ratio of SAMW and

320 AAIW, water masses of near-global importance that are subducted from the SAZ and ventilate the basal-

321 thermocline and intermediate ocean (Hanawa and Talley, 2001; Sallée et al., 2010), as previously

322 suggested by Ellwood (2008) and Wyatt et al. (2014). Indeed, in our OGCM simulations, the Zn:Si ratio

323 along an isopycnal corresponding to SAMW in the Atlantic Ocean ($\sigma_\theta = 26.8$ kg/m^3), which outcrops

324 in the SAZ near 45°S in the OGCM, responds sensitively to the $r_{Zn:P}$ value of Southern Ocean uptake:

325 as with the Subantarctic surface from which it is ventilated, the Zn:Si ratio on this isopycnal falls to

326 values close the mean-ocean ratio with elevated Southern Ocean Zn uptake. This ratio also correlates

327 exceptionally strongly with the root-mean-square difference between the global Zn and Si distributions

328 ($r^2 = 0.99$; Fig. S7): the marine Zn and Si distributions are most similar when the Zn:Si ratio on this

329 isopycnal is closest to the mean-ocean ratio. Taken together, these interrelationships show that the

330 biogeochemical properties of the upper-ocean water masses ventilated from the SAZ are the decisive

331 element in creating a close correlation between the global marine Zn and Si distributions, by transposing

332 the low- Zn, low-Si signature of the surface SAZ into the interior.

333 **3.4. General systematics of the Subantarctic control**

334 The discussion in Sections 3.2 and 3.3 above has clearly shown the importance of Subantarctic surface

335 properties for the global Zn distribution, and the physical mechanism by which this control comes about.

336 We now attempt to gain a more generalised understanding of the Subantarctic control on the large-scale

337 distribution of Zn and biologically-cycled elements in general.

338 We first consider the biological drawdown of Zn and PO$_4$ in the surface Southern Ocean. Results

339 discussed in Section 3.2 demonstrated that it is Zn-depletion in the Subantarctic that is key to

340 reproducing the observed Zn–Si correlation. We apply a simple generalised framework to assess the

341 relative Southern Ocean drawdown of Zn and PO$_4$ simulated by our sensitivity suite, building upon the

342 fact that PO$_4$ concentrations in the Subantarctic Zone are only ~40% of those in Antarctic waters south

343 of the Polar Front (Garcia et al., 2013). If we make the simplifying assumption that all nutrient supply

344 to the SAZ comes through Ekman transport from the south, then in order to produce a Subantarctic

345   surface depleted in Zn, Southern Ocean Zn drawdown must be sufficiently strong to produce Zn-

346   depletion when PO_4 has been drawn down to only 40% of its initial Antarctic value. We thus calculate

347   the expected relationship between the drawdown of Zn and PO_4 that results from the parameter choices

348   for the equation governing $r_{Zn:P}$ (Eqn. 1) in our OGCM sensitivity suite. In Fig. 8, it can be seen that

349   when PO_4 has been drawn down to 40% of its initial Antarctic concentration, the simulated fraction of

350   residual Zn varies between ~0% and ~60%. Those simulations that draw down Zn most strongly (G11,

351   *aHI-cLO*, *aHI-cHI*), depleting Zn when residual PO_4 is at 40% or more, best reproduce the observed

352   covariation between Zn and PO_4 in the surface Southern Ocean (Fig. 8; Zhao et al., 2014). Tellingly, it

353   is these same simulations that best reproduce the global linear relationship between Zn and Si (Fig. 2).

354   This general framework thus shows that a key variable in determining Subantarctic Zn status, and thus

355   the large-scale Zn distribution, is the *integrated* Zn:PO_4 uptake ratio experienced by surface Southern

356   Ocean water masses as they are transported northwards to the Subantarctic Zone.

357   Secondly, whilst in the case of Zn it is *depletion* in the Subantarctic surface that is a key prerequisite to

358   correctly simulating the Zn–Si and Zn–PO_4 relationships, the systematics of our box-model ensemble

359   offer the tantalising suggestion that this might be only one specific case of a coupled biological-physical

360   Subantarctic mechanism that explains elemental correlations in the sea more generally. As discussed in

361   Section 3.3, box-model simulations in which high $r_{Zn:P}$ values lead to strong Zn drawdown have a

362   Subantarctic Zn:Si ratio very similar to the global-ocean mean (Fig. 7a), and hence strongly correlated

363   Zn and Si distributions. Analysis of the Zn:PO_4 systematics of the ensemble shows that the simulated

364   Zn distribution becomes, instead, almost perfectly linearly correlated with PO_4 when the Zn:PO_4 ratio

365   in the SAZ equals the mean-ocean Zn:PO_4 ratio of ~2.5 mmol/mol (Fig. S8). The analogous existence

366   of such a link between Subantarctic elemental stoichiometry and global distributions for both Zn–Si *and*

367   Zn–PO_4 suggests a more general mechanism of Subantarctic control. The ventilation of the upper-ocean

368   water masses SAMW and AAIW from the Subantarctic introduces its surface stoichiometric signal into

369   the ocean interior, setting the preformed stoichiometry of the upper ocean (Fig. 9). If this upper-ocean

370   "endmember", with low elemental concentrations, bears the same stoichiometric ratio between two

371   elements as the nutrient-rich deep ocean that influences the global mean, the global relationship between

372   these two elements will be near-linear (Fig. 9), as in the case of Zn and Si in the modern ocean. If, in

14

373   contrast, Southern Ocean uptake leads to a strong relative depletion in one of these elements in the

374   Subantarctic surface, the low-concentration endmember subducted from the Subantarctic will bear a

375   lower elemental ratio than the nutrient-rich deep ocean, a ratio that is imparted not only to the

376   thermocline but also to the formation regions of nutrient-poor North Atlantic Deep Water, via the cross-

377   equatorial transport of SAMW/AAIW (de Souza et al., 2015). As a result, the global relationship

378   between the two elements will be convex-upwards (Fig. 9), with a steep relationship representing mixing

379   between Subantarctic-sourced upper-ocean waters and the nutrient-rich deep ocean – as in the case of

380   Zn and PO_4 in the ocean (Fig. S3) or, indeed, Si and PO_4.

381   **3.5. Synthesis and broader implications**

382   The discussion above has highlighted the extent to which Southern Ocean Zn uptake plays a role in

383   determining the global Zn distribution. Specifically, the OGCM results presented in Section 3.2 show

384   that the northward extension of elevated Zn uptake into the SAZ, even as Zn and Zn^{2+} concentrations

385   drop, is key to reproducing the observed Zn–Si correlation (Fig. 4). It must be noted that our

386   biogeochemical model achieves this uptake via a relationship between Zn:PO_4 uptake ratios and Zn^{2+}

387   (Eqn. 1) that is certainly an oversimplification of the complexity of marine Zn biogeochemistry (e.g.

388   Varela et al., 2011). The surface distribution of Zn^{2+} is sensitive to the concentration and distribution of

389   the chelating ligand that binds most dissolved Zn. Ligand-sensitivity simulations show that the specifics

390   of our results are dependent on the absolute value of this parameter (Fig. S10). However, our analysis

391   has focused on the systematics of our sensitivity suite, which is unaffected by such specifics (Fig. S10).

392   This approach has allowed us to identify macro-scale biogeochemical processes that are associated with

393   the simulation of a more realistic marine Zn distribution, and it is on this process understanding that we

394   focus here.

395   Whilst at the global scale the production of a Zn-depleted Subantarctic surface seems to be a sufficient

396   condition for reproducing the Zn distribution, at the regional scale additional nuances appear.

397   Simulations *aHI-cLO* and *aHI-cHI*, for instance, demonstrate similar global skill (Fig. 2c,d), and both

398   produce a Zn-depleted Subantarctic surface, although Zn drawdown in *aHI-cHI* is considerably stronger

399   than in *aHI-cLO* (Fig. 8c), as a result of the extremely high $r_{Zn:P}$ that *aHI-cHI* simulates at high Zn^{2+}

400   concentrations (Fig. 8d). This elevated Zn uptake has consequences for the latitudinal distribution of Zn

15

401   in the surface Southern Ocean simulated by *aHI-cHI*, limiting the degree to which Zn concentrations

402   can rise in regions of Southern Ocean upwelling centred around 60°S (Fig. 6). Thus unlike *aHI-cLO*,

403   which reproduces the observed surface Southern Ocean covariation between Zn and Si along the prime

404   meridian (Zhao et al., 2014) with good fidelity, *aHI-cHI* consistently underestimates Zn concentrations

405   in the far south (Fig. S9). This difference in regional skill suggests that the step-like increase in $r_{Zn:P}$

406   simulated by *aHI-cLO*, with low values in the temperate latitudes and a rapid rise to a plateau of high

407    $r_{Zn:P}$ values in the subpolar and polar oceans, better captures the variation of $r_{Zn:P}$ required to explain the

408   Zn distribution at multiple scales, ranging from the regional to the global. Our simple biogeochemical

409   model produces this step via what is essentially a physiological mechanism (Eqn. 1), but the sharp

410   separation of oceanic provinces that results suggests the possibility that such a variation might, in the

411   real ocean, be driven instead by differences in biogeography, nutrient status or environmental

412   conditions.

413   Differing Zn quotas in high- and low-latitude phytoplankton could, for instance, be the result of adaptive

414   changes to ambient Zn concentrations within phytoplankton groups, analogous to differences in Si quota

415   observed between high-latitude and equatorial diatoms (e.g. Baines et al., 2010); such an adaptation is

416   indeed suggested by the lower Zn requirements observed in open-ocean phytoplankton species relative

417   to coastal ones (Sunda and Huntsman, 1992). Alternatively, as has been previously suggested by

418   Ellwood (2008) and Croot et al. (2011), elevated Zn quotas in high-latitude high-nutrient low-

419   chlorophyll regions such as the Southern Ocean and subpolar North Pacific may be a response to the

420   chronic iron limitation of phytoplankton in these regions (Chisholm and Morel, 1991), since iron

421   limitation has been shown to elevate Zn quotas in iron-limited natural phytoplankton communities

422   (Sunda and Huntsman, 2000; Cullen et al., 2003). Our biogeochemical model, with its prescribed

423   dependency of $r_{Zn:P}$ on Zn^{2+}, is by construction agnostic as to the ecological and/or biochemical causes

424   of the variation in $r_{Zn:P}$. What is clear is that model variants that produce a realistic Zn distribution also

425   reproduce the marked difference in Zn quotas observed between Southern Ocean diatoms and low-

426   latitude genera (Twining and Baines, 2013). In our opinion, this result strongly suggests that it is

427   Southern Ocean diatoms that are dominantly responsible for the large-scale Zn-Si correlation in the

428   global ocean (see also Ellwood, 2008), and that – via their extraordinary affinity for Zn and abundant

429 seasonal blooms – they dominantly control the fluxes driving the global-scale Zn cycle. Certainly, in

430 our most skilful model variants, Zn export fluxes south of 40°S represent 44% or more of global Zn

431 export (Table S2), making the Southern Ocean almost as important for Zn as for Si (54%), and more

432 than twice as important as for the export of P (19%). In this context, it is worth re-iterating that the

433 observed levels of Zn directly incorporated into the opaline frustules of diatoms are too low to explain

434 the marine Zn–Si correlation, as shown by simulations of coupled Zn-Si cycling discussed in the

435 Supplementary Information.

436 The far-reaching consequences of elevated Southern Ocean Zn uptake are highlighted by fact that the

437 physical model we employ simulates significant low-latitude upwelling (Resplandy et al., 2016). This

438 simulated upwelling is patently insufficient to overcome the Zn depletion of the upper ocean that results

439 when Zn is stripped out of the model's SAZ. With most Zn efficiently trapped in the deep ocean by the

440 elevated Zn export fluxes of the Southern Ocean, wind-driven upwelling in coastal and equatorial

441 regions can only tap into a relatively small Zn upper-ocean pool, most of which is likely efficiently

442 recycled within the upper ocean due to the shallow remineralisation of organic-associated Zn (Twining

443 et al., 2014). It would thus seem that the low-latitude cycling of Zn is dominated by a shallow recycling

444 loop that remains rather disconnected from the large-scale, Southern-Ocean-dominated cycle

445 determining the global Zn distribution. This raises the interesting possibility that the observed

446 differences between the Zn quotas of eukaryotic and prokaryotic phytoplankton (e.g. Sunda and

447 Huntsman, 1992, 1995; Saito et al., 2002; Twining et al., 2011) may also be the consequence of

448 adaptation to ambient Zn concentrations, rather than representing a fundamental physiological

449 difference: by sequestering Zn in the deep Southern Ocean, high-latitude eukaryotic diatom

450 communities might effectively "starve" low-latitude phytoplankton communities, including prokaryotic

451 cyanobacteria that thrive in the subtropics, of zinc. Whilst speculative, it appears at least possible that

452 the lower Zn quotas observed for low-latitude cyanobacteria (e.g. Twining et al., 2011) might represent

453 an adaptive response to this diatom-driven Zn starvation, rather than reflecting a fundamental difference

454 in physiological demand between prokaryotes and eukaryotes (cf. Saito et al., 2003).

455 At the broadest scale, the correlative mechanism identified by this study has applicability beyond the

456 marine Zn distribution. As discussed in detail in Section 3.4, the degree to which Southern Ocean uptake

457 draws down the Subantarctic concentration of an element relative to that of PO_4 determines the upper-

458 ocean endmember that defines the interior-ocean correlation between that element and PO_4 (Fig. 9). This

459 mechanism should apply equally to other elements whose oceanic residence time is sufficiently long for

460 large-scale circulation to play a significant role in determining their distribution. In this context, the

461 much-discussed "kink" in the marine relationship between cadmium (Cd) and PO_4 would appear to

462 result from Southern Ocean uptake that is elevated in Cd relative to PO_4, albeit to a smaller extent than

463 is the case for Zn (cf. Baars et al., 2014). Further observations of *in situ* utilisation and phytoplankton

464 stoichiometry, as well as modelling studies of their effects on the large-scale distribution, would allow

465 a robust test of this hypothesis.

466 **4. Conclusions**

467 Vance et al. (2017) recently showed that elevated Southern Ocean uptake of Zn can produce the

468 observed correlation between the global distributions of dissolved Zn and Si in seawater without any

469 mechanistic links between their marine cycles. In this study, our interest has been to understand the main

470 biological and physical mechanisms through which surface uptake in the remote Southern Ocean

471 exercises such global influence. Our model sensitivity suites have shown that the stoichiometry of

472 Southern Ocean Zn uptake relative to that of PO_4 controls the degree of similarity between Zn and Si

473 distributions via its influence on the elemental stoichiometry of the Subantarctic Zone of the Southern

474 Ocean, where water masses that fill the upper ocean are formed. Because both Si and Zn are drawn

475 down nearly to completion before being subducted into the upper-ocean interior by SAMW/AAIW, the

476 global ocean Zn-Si relationship comes to resemble a simple mixing line between the Zn- and Si-depleted

477 SAMW/AAIW endmember and the high-Zn and high-Si deep ocean, with the mean ocean Zn:Si ratio

478 determining the slope of the relationship. Furthermore, since the upper ocean holds very little of the

479 global ocean Zn and Si inventories, the global-scale correlation set in the frontal system of the Southern

480 Ocean cannot be undone by biological cycling in the low-latitude surface, or by differences in the

481 remineralisation depths of Zn-bearing organic matter and opal.

482

483 *Acknowledgements*

489

References

491 Baars, O., Croot, P.L., 2011. The speciation of dissolved zinc in the Atlantic sector of the Southern
492   Ocean. *Deep Sea Res. II* 58, 2720-2732.

493 Baars, O., Abouchami, W., Galer, S.J.G., Boye, M., Croot, P.L., 2014. Dissolved cadmium in the
494   Southern Ocean: distribution, speciation, and relation to phosphate. *Limnol. Oceanogr.* 59, 385-399.

495 Baines, S.B., Twining, B.S., Brzezinski, M.A., Nelson, D.M., Fisher, N.S., 2010. Causes and
496   biogeochemical implications of regional differences in silicification of marine diatoms. *Glob.*
497   *Biogeochem. Cyc. 24*, GB4031, doi: 10.1029/2010gb003856.

498 Broecker, W.S., Peng, T.H., 1982. *Tracers in the Sea.* Eldigio Press/Lamont-Doherty Geological
499   Observatory, Palisades, NY.

500 Bruland, K.W., 1980. Oceanographic distributions of cadmium, zinc, nickel, and copper in the North
501   Pacific. *Earth Planet. Sci. Lett.* 47, 176-198.

502 Bruland, K.W., 1989, Complexation of zinc by natural organic ligands in the central North Pacific.
503   *Limnol. Oceanogr.* 34, 269-285.

504 Chester, R., Jickells, T., 2012. *Marine Geochemistry*, 3rd ed. Wiley-Blackwell, Chichester.

505 Chisholm, S.W., Morel, F.M.M. (eds.), 1991. Special Issue: What controls phytoplankton production in
506   nutrient-rich areas of the open sea? *Limnol. Oceanogr.* 36, 1507-1970.

507 Croot, P.L., Baars, O., Streu, P., 2011. The distribution of dissolved zinc in the Atlantic sector of the
508   Southern Ocean. *Deep-Sea Res. II* 58, 2707-2719.

509 Cullen, J.T., Chase, Z., Coale, K.H., Fitzwater, S.E., Sherrell, R.M., 2003. Effect of iron limitation on
510   the cadmium to phosphorus ratio of natural phytoplankton assemblages from the Southern Ocean.
511   *Limnol. Oceanogr.* 48, 1079-1087.

512 de Souza, G.F., Slater, R.D., Hain, M.P., Brzezinski, M.A., Sarmiento, J. L., 2015. Distal and proximal
513   controls on the silicon stable isotope signature of North Atlantic Deep Water. *Earth Planet. Sci. Lett.*
514   432, 342-353.

515 Donat, J.R., Bruland, K.W., 1990. A comparison of two voltammetric techniques for determining zinc
516   speciation in Northeast Pacific Ocean waters. *Mar. Chem.* 28, 301-323.

517 Ellwood, M.J., 2004. Zinc and cadmium speciation in Subantarctic waters east of New Zealand. *Mar.*
518   *Chem.* 87, 37-58.

519   Ellwood, M.J., 2008. Wintertime trace metal (Zn, Cu, Ni, Cd, Pb and Co) and nutrient distributions in
520   the Subantarctic Zone between 40-52°S; 155-160°E. *Mar. Chem.* 112, 107-117.

521   Ellwood, M.J., Hunter, K.A., 2000. The incorporation of zinc and iron into the frustule of the marine
522   diatom *Thalassiosira pseudonana. Limnol. Oceanogr.* 45, 1517-1524.

523   Garcia, H.E., Locarnini, R.A., Boyer, T.P., Antonov, J.I., Baranova, O.K., Zweng, M.M., et al., 2013.
524   *World Ocean Atlas 2013, Volume 4: Dissolved Inorganic Nutrients (phosphate, nitrate, silicate)*, in:
525   Levitus, S. (Ed.), NOAA Atlas NESDIS, Silver Spring, MD, p. 25.

526   Hain, M.P., Sigman, D.M., Haug, G.H., 2014. Distinct roles of the Southern Ocean and North Atlantic
527   in the deglacial atmospheric radiocarbon decline. *Earth Planet. Sci. Lett.* 394, 198-208.

528   Hanawa, K., Talley, L.D., 2001. *Mode waters*, in: Siedler, G., Church, J.A., Gould, J. (Eds.), Ocean
529   circulation and climate -- observing and modelling the global ocean. Academic Press, San Diego, pp.
530   373-386.

531   Keir, R.S., 1988. On the Late Pleistocene ocean geochemistry and circulation. *Paleoceanogr.* 3, 413-
532   455.

533   Khatiwala, S., Visbeck, M., Cane, M.A., 2005. Accelerated simulation of passive tracers in ocean
534   circulation models. *Oc. Modell.* 9, 51-69.

535   Lohan, M.C., Crawford, D.W., Purdie, D.A., Statham, P.J., 2005. Iron and zinc enrichments in the
536   northeastern subarctic Pacific: ligand production and zinc availability in response to phytoplankton
537   growth. *Limnol. Oceanogr.* 50, 1427-1437.

538   Marshall, J., Adcroft, A., Hill, C., Perelman, L., Heisey, C., 1997. A finite-volume, incompressible
539   Navier-Stokes model for studies of the ocean on parallel computers. *J. Geophys. Res. Ocean.* 102,
540   5733-5752.

541   Mawji, E., Schlitzer, R., Dodas, E.M., Abadie, C., Abouchami, W., Anderson, R.F., et al., 2015. The
542   GEOTRACES Intermediate Data Product 2014. *Mar. Chem.* 177, 1-8.

543   Morel, F.M.M., Milligan, A.J., Saito, M.A., 2014. *Marine bioinorganic chemistry: the role of trace
544   metals in the oceanic cycles of major nutrients,* in: Holland, H.D., Turekian, K.K. (Eds.), Treatise on
545   Geochemistry (Second Edition). Elsevier, Oxford, pp. 123-150.

546   Najjar, R.G., Jin, X., Louanchi, F., Aumont, O., Caldeira, K., Doney, S.C., et al., 2007. Impact of
547   circulation on export production, dissolved organic matter, and dissolved oxygen in the ocean: Results
548   from Phase II of the Ocean Carbon-cycle Model Intercomparison Project (OCMIP-2). *Glob.
549   Biogeochem. Cyc.* 21, doi: 10.1029/2006gb002857.

550   Price, J., Badger, M.R., 1989. Isolation and characterization of high CO_2-requiring mutants of the
551   cyanobacterium *Synechococcus* PCC7942-2 phenotypes that accumulate inorganic carbon but are
552   apparently unable to generate CO_2 within the carboxysome. *Plant Physiol.* 91, 514-525.

553   Resplandy, L., Keeling, R.F., Stephens, B.B., Bent, J.D., Jacobson, A., Rödenbeck, C., Khatiwala, S.,
554   2016. Constraints on oceanic meridional heat transport from combined measurements of oxygen and
555   carbon. *Clim. Dyn.* 47, 3335-3357.

556   Rueter, J.G., Morel, F.M.M., 1981. The interaction between zinc deficiency and copper toxicity as it
557   affects the silicic acid uptake mechanisms in *Thalassiosira pseudonana*. *Limnol. Oceanogr.* 26, 67-
558   73.

559   Saito, M.A., Moffett, J.W., Chisholm, S.W., Waterbury, J.B., 2002. Cobalt limitation and uptake in
560   *Prochlorococcus*. *Limnol. Oceanogr.* 47, 1629-1636.

561   Saito, M.A., Sigman, D.M., Morel, F.M.M., 2003. The bioinorganic chemistry of the ancient ocean: the
562   co-evolution of cyanobacterial metal requirements and biogeochemical cycles at the Archean-
563   Proterozoic boundary. *Inorg. Chim. Acta* 356, 308-318.

564   Sallée, J.-B., Speer, K., Rintoul, S., Wijffels, S., 2010. Southern Ocean thermocline ventilation. *J. Phys.
565   Oceanogr.* 40, 509-529.

566   Sarmiento, J.L., Simeon, J., Gnanadesikan, A., Gruber, N., Key, R.M., Schlitzer, R., 2007. Deep ocean
567   biogeochemistry of silicic acid and nitrate. *Glob. Biogeochem. Cyc.* 21, doi: 10.1029/2006GB002720.

568   Sherbakova, T.A., Masyukova, Y.A., Safonova, T.A., Petrova, D.P., Vereshagin, A.L., Minaeva, T.V.,
569   et al., 2005. Conserved motif CMLD in silicic acid transport proteins of diatoms. *Mol. Biol.* 39, 269-
570   280.

571   Sigman, D.M., DiFiore, P.J., Hain, M.P., Deutsch, C., Wang, Y., Karl, D.M., et al., 2009. The dual
572   isotopes of deep nitrogen as a constraint on the cycle and budget of oceanic fixed nitrogen. *Deep-Sea
573   Res. I* 56, 1419-1439.

574   Sunda, W.G., Huntsman, S.A., 1992. Feedback interactions between zinc and phytoplankton in
575   seawater. *Limnol. Oceanogr.* 37, 25-40.

576   Sunda, W.G., Huntsman, S.A., 1995. Cobalt and zinc interreplacement in marine phytoplankton:
577   biological and geochemical implications. *Limnol. Oceanogr.* 40, 1404-1417.

578   Sunda, W.G., Huntsman, S.A., 2000. Effect of Zn, Mn, and Fe on Cd accumulation in phytoplankton:
579   Implications for oceanic Cd cycling. *Limnol. Oceanogr.* 45, 1501-1516.

580   Taylor, K.E., 2001. Summarizing multiple aspects of model performance in a single diagram. *J.
581   Geophys. Res. Atmos.* 106, 7183-7192.

582   Twining, B.S., Baines, S.B., Fisher, N.S., 2004. Element stoichiometries of individual plankton cells
583   collected during the Southern Ocean Iron Experiment (SOFeX). *Limnol. Oceanogr.* 49, 2115-2128.

584   Twining, B.S., Baines, S.B., Bozard, J.B., Vogt, S., Walker, E.A., Nelson, D.M., 2011. Metal quotas of
585   plankton in the equatorial Pacific Ocean. *Deep-Sea Res. II* 58, 325-341.

586   Twining, B.S., Baines, S.B., 2013. The trace metal composition of marine phytoplankton. *Ann. Rev.
587   Mar. Sci. 5*, 191-215.

588   Twining, B.S., Nodder, S.D., King, A.L., Hutchins, D.A., LeCleir, G.R., DeBruyn, J.M., et al., 2014.
589   Differential remineralization of major and trace elements in sinking diatoms. *Limnol. Oceanogr.* 59,
590   689-704.

591   Vance, D., Little, S.H., de Souza, G.F., Khatiwala, S., Lohan, M.C., Middag, R., 2017. Silicon and zinc
592   biogeochemical cycles coupled through the Southern Ocean. *Nature Geosci.,* doi: 10.1038/ngeo2890.

593 Varela, D.E., Willers, V., Crawford, D.W., 2011. Effect of zinc availability on growth, morphology, and
594   nutrient incorporation in a coastal and an oceanic diatom. *J. Phycol.* 47, 302-312.

595 Wyatt, N.J., Milne, A., Woodward, A.M.E., Rees, A.P., Browning, T.J., Bouman, H.A., Worsfold, P.J.,
596   Lohan, M.C., 2014. Biogeochemical cycling of dissolved zinc along the GEOTRACES South Atlantic
597   transect GA10 at 40°S. *Glob. Biogeochem. Cyc.* 28, doi: 10.1002/2013GB004637.

598 Zhao, Y., Vance, D., Abouchami, W., de Baar, H.J.W., 2014. Biogeochemical cycling of zinc and its
599   isotopes in the Southern Ocean. *Geochim. Cosmochim. Acta* 125, 653-672.

601

602 **Fig. 1:** Stoichiometry of simulated uptake. Panel *a* shows the dependence of the Zn:P uptake ratio $r_{Zn:P}$

603 on the ambient concentration of Zn^{2+} observed in culture experiments by Sunda and Huntsman (1992).

604 Data in Sunda and Huntsman (given as Zn:C ratios) have been converted to Zn:P using the Redfield C:P

605 ratio of 106 mol/mol. Panel *b* schematically illustrates the influence of the parameters a_{Zn}, b_{Zn} and c_{Zn} in

606 Eqn. 1 on the shape of this dependency.
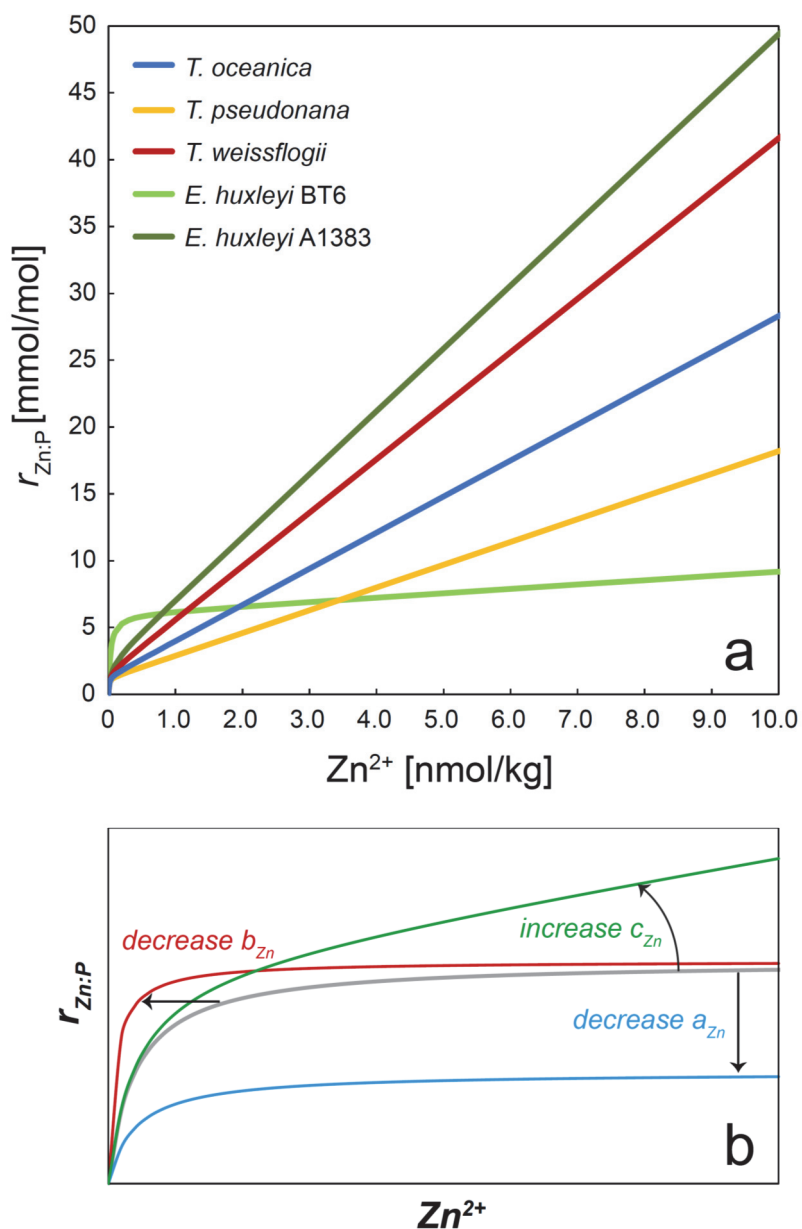
607

608

609 **Fig. 2:** Taylor diagrams illustrating the degree of similarity between the simulated Zn field and (a,c) the
610 simulated Si field or (b,d) the simulated PO_4 field. Upper panels show results for the base set of
611 simulations G1-G11; lower panels show results for the simulations G21-G24 (simulations G9 and G11
612 are included as reference). The pink star in panel *b* represents the similarity between simulated Si and
613 PO_4 fields for reference. The bulls-eye symbol at (1,1) represents the point at which both fields being
614 compared are statistically identical.

615
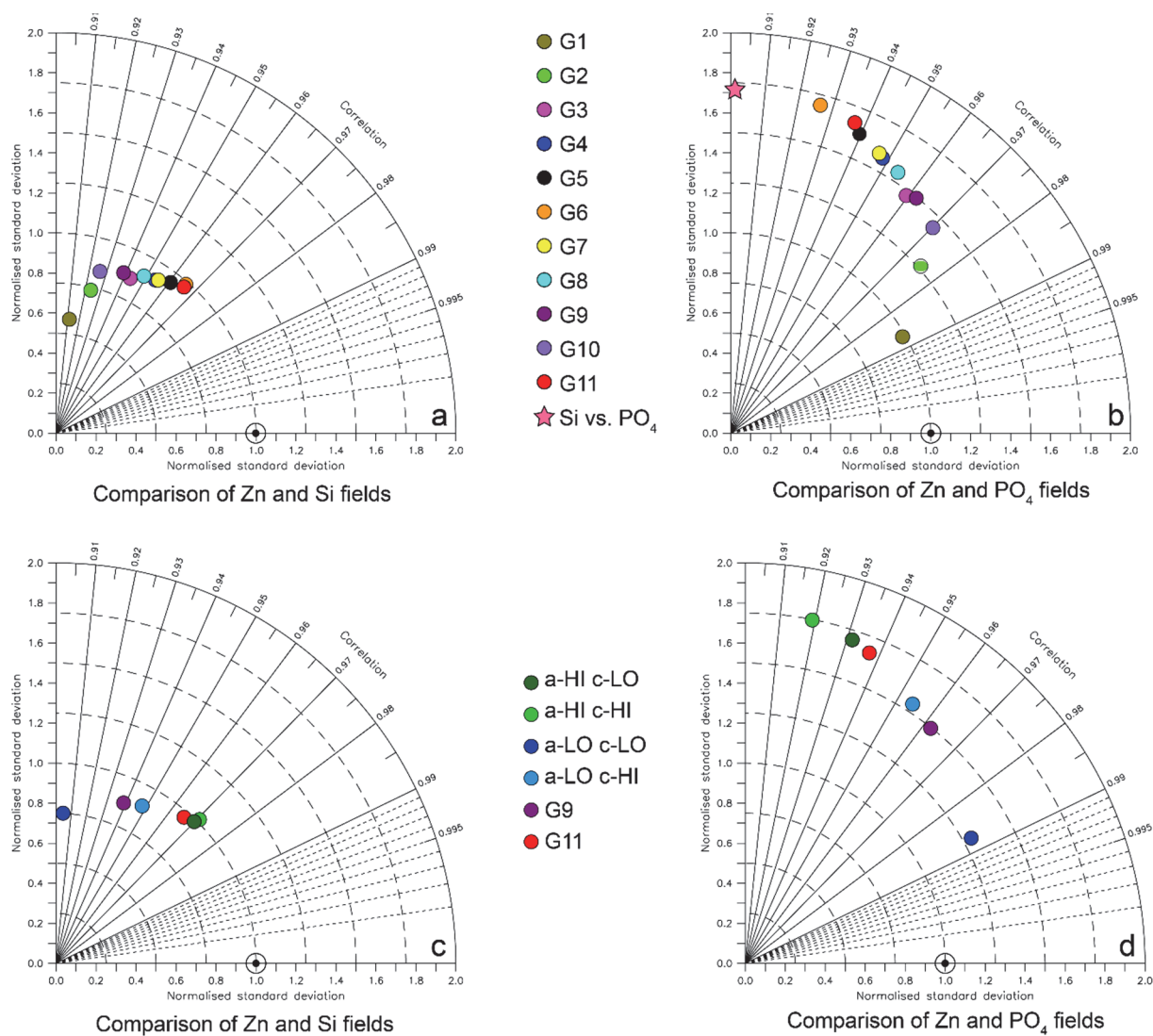
Fig. 3: Basin-average depth profiles produced by (a-d) simulation G11, in which the global Zn–Si relationship is well reproduced. The preferential shallow remineralisation of Zn is visible in all profiles, but only as a minor enrichment of Zn relative to Si in the upper ocean. In panel *a*, the basin-average PO_4 profile for the Atlantic basin is also shown, in order to show the degree of difference between the Zn and PO_4 fields, despite the fact that our model couples their uptake and regeneration (see Section 2 of the main text). Panels *e-h* present observational data for selected stations within each ocean basin for comparison. Data are from Bruland et al. (1980), Zhao et al. (2014) and Mawji et al. (2015).
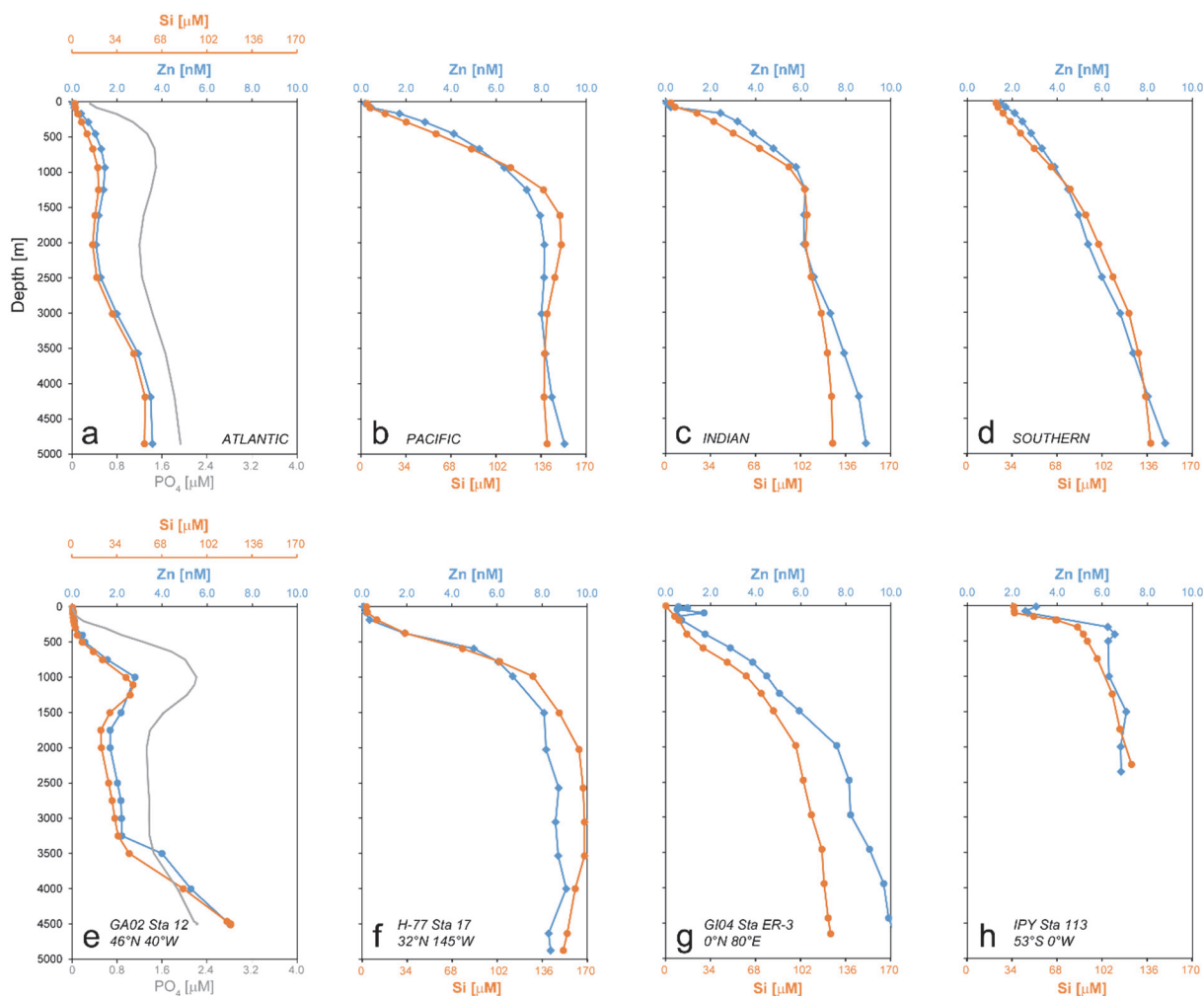
**Fig. 4:** Maps of (a,b) surface Zn concentration, (c,d) Zn:PO$_4$ uptake ratio, and (e,f) surface Zn:Si ratio in simulation G10 (left panels) and G11 (right panels). Simulation G10 is less skilful at reproducing a Si-like Zn distribution than G11 (Fig. 2), reflected e.g. by the elevation of surface Zn concentrations in the eastern equatorial Pacific Ocean (panel *a*). Panel *c* shows the relatively low Zn:PO$_4$ uptake ratios simulated by G10 in the high-latitude oceans, in contrast to the high ratios in simulation G11 (panel *d*). As a result, G10 shows a strong increase in the Zn:Si ratio from the Antarctic to the Subantarctic zone (panel *e*), whereas the surface Southern Ocean has a relatively homogeneous Zn:Si ratio in G11 (panel *f*). The Subantarctic Zone is indicated by white stippling in panels *e* and *f*.
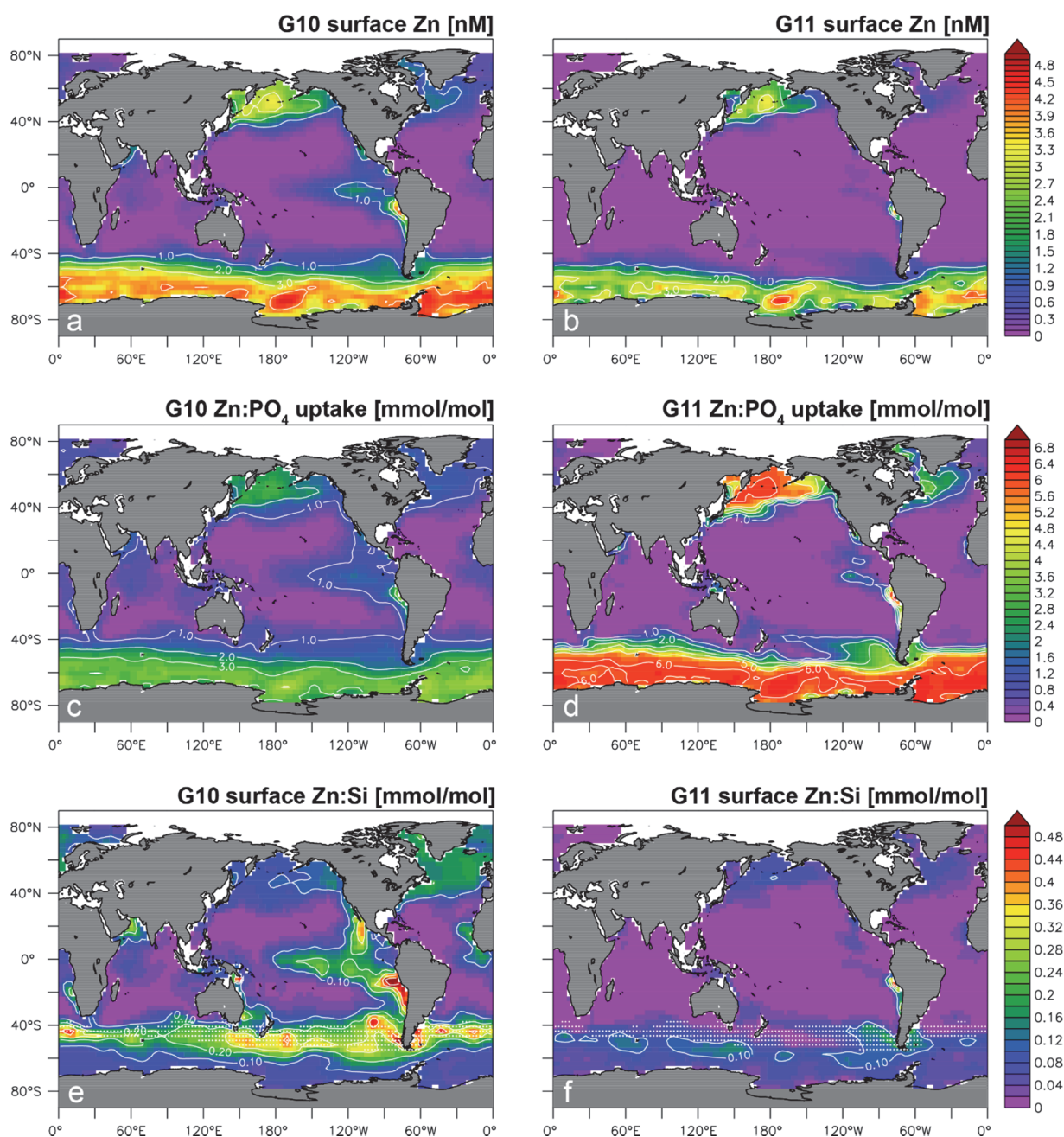
Fig. 5: Maps of Zn:PO₄ uptake ratios in simulations G21-G24, illustrating the effects of varying parameters a_{Zn} and c_{Zn} of Eqn. 1. It can be seen that whilst a high c_{Zn} -value can lead to elevated uptake at high latitudes (panels *a,b*), only a high a_{Zn}-value produces a step-like increase in the Subantarctic Ocean (panels *c,d*). The Subantarctic Zone is indicated by white stippling.
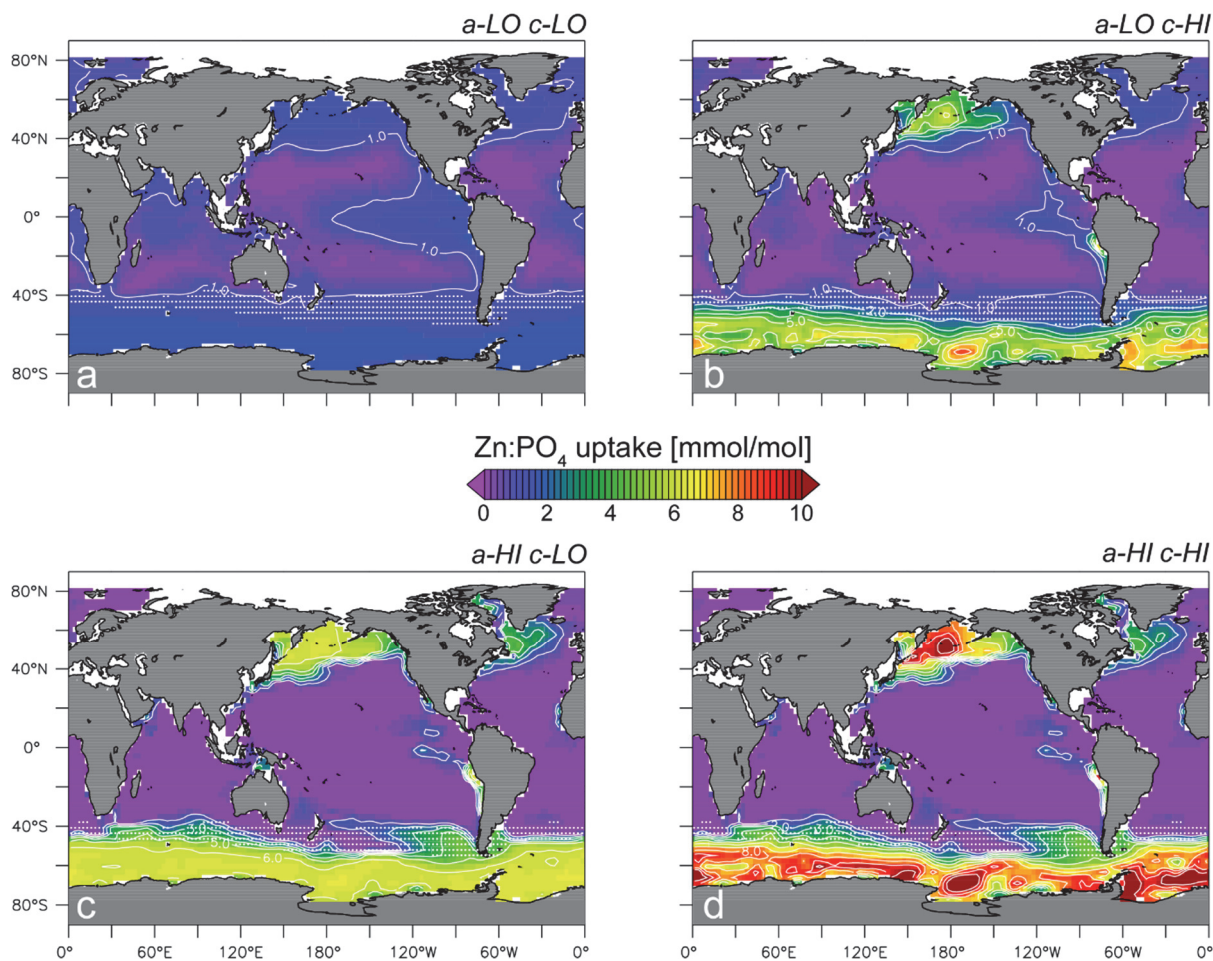
Fig. 6: Zonal average surface Zn concentrations simulated in G21-G24, in which the values of parameters a_{Zn} and c_{Zn} of Eqn. 1 are systematically varied. Dashed grey lines represent two endmember behaviours in which Zn behaves exactly like either PO_4 or Si, produced by scaling the simulated surface PO_4 (or Si) distribution by the $Zn:PO_4$ (or $Zn:Si$) ratio of the oceanic inventories. The difference between simulation *aHI-cLO* and *aLO-cLO* shows the influence of elevated values of a_{Zn} on the surface Zn distribution, resulting in a decrease of Zn concentrations in the Subantarctic Zone (~40-50°S) to low values and a poleward migration of the meridional Zn gradients between the high- and mid-latitudes.
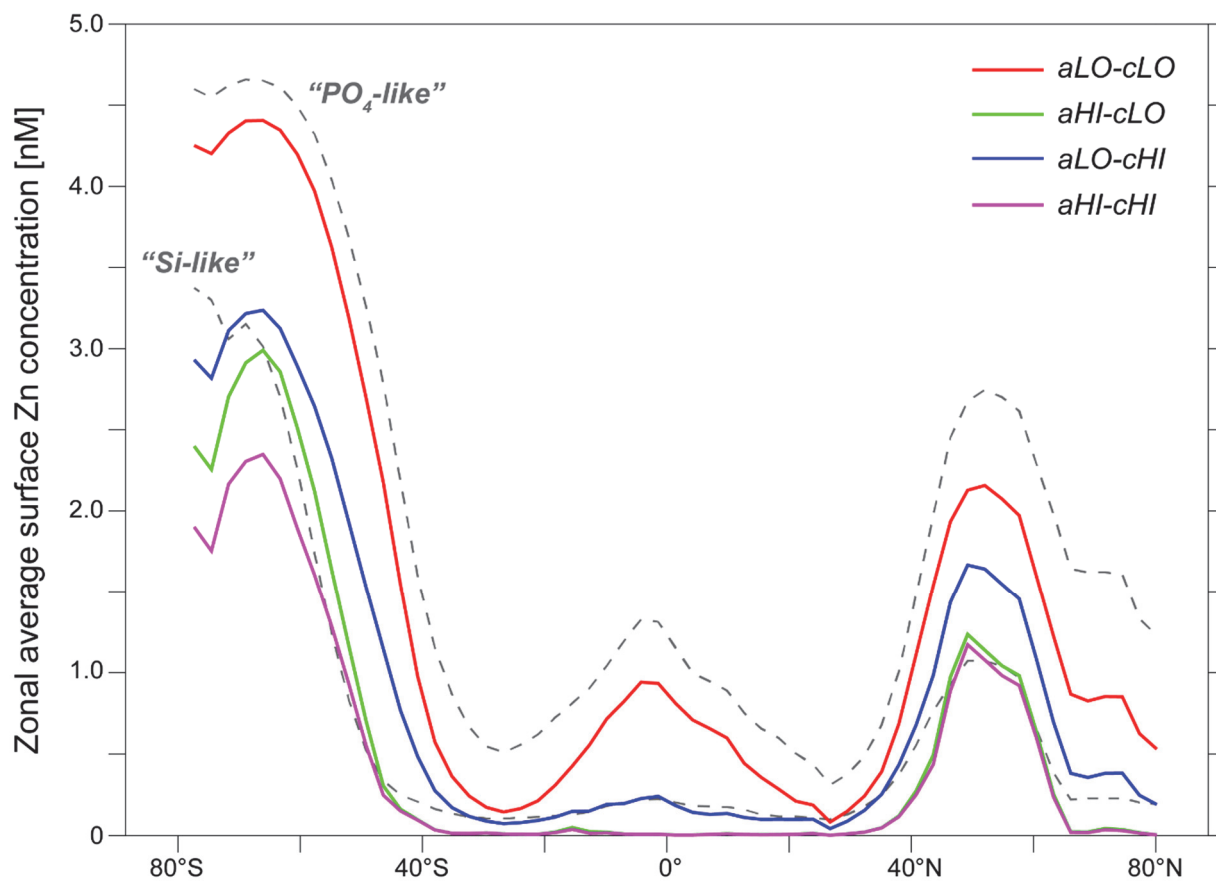
Fig. 7: Sensitivity simulation systematics in (a,c,e) the box-model ensemble and (b,d,f) OGCM simulations (G1-G11,G21-G24). Box-model ensemble results are shown as density maps of the percentage of ensemble members with the given *x,y* characteristics. Panels *a* and *b* show that higher Southern Ocean Zn:PO$_4$ uptake (i.e. the model's Antarctic and Subantarctic boxes) results in a steady decrease in Zn:Si in Subantarctic waters, with values approaching the global-ocean mean (dashed line) when Southern Ocean Zn:PO$_4$ uptake is ~5.5 mmol/mol. Vertical grey bars mark the range of Southern Ocean $r_{Zn:P}$ that produce a SAZ Zn:Si ratio close to the global-ocean mean. Panels *c* and *d* show metrics for the similarity between the resulting Zn and Si tracer fields (correlation coefficient r^2 or normalised centred root-mean-square difference $\hat{E}'$, defined in Table 1; note reversed *y*-axis in *d* and *e*). Panels *e* and *f* show that as the surface Subantarctic Zn:Si approaches the global mean, the similarity between the simulated Zn and Si tracer fields increases towards its highest values.
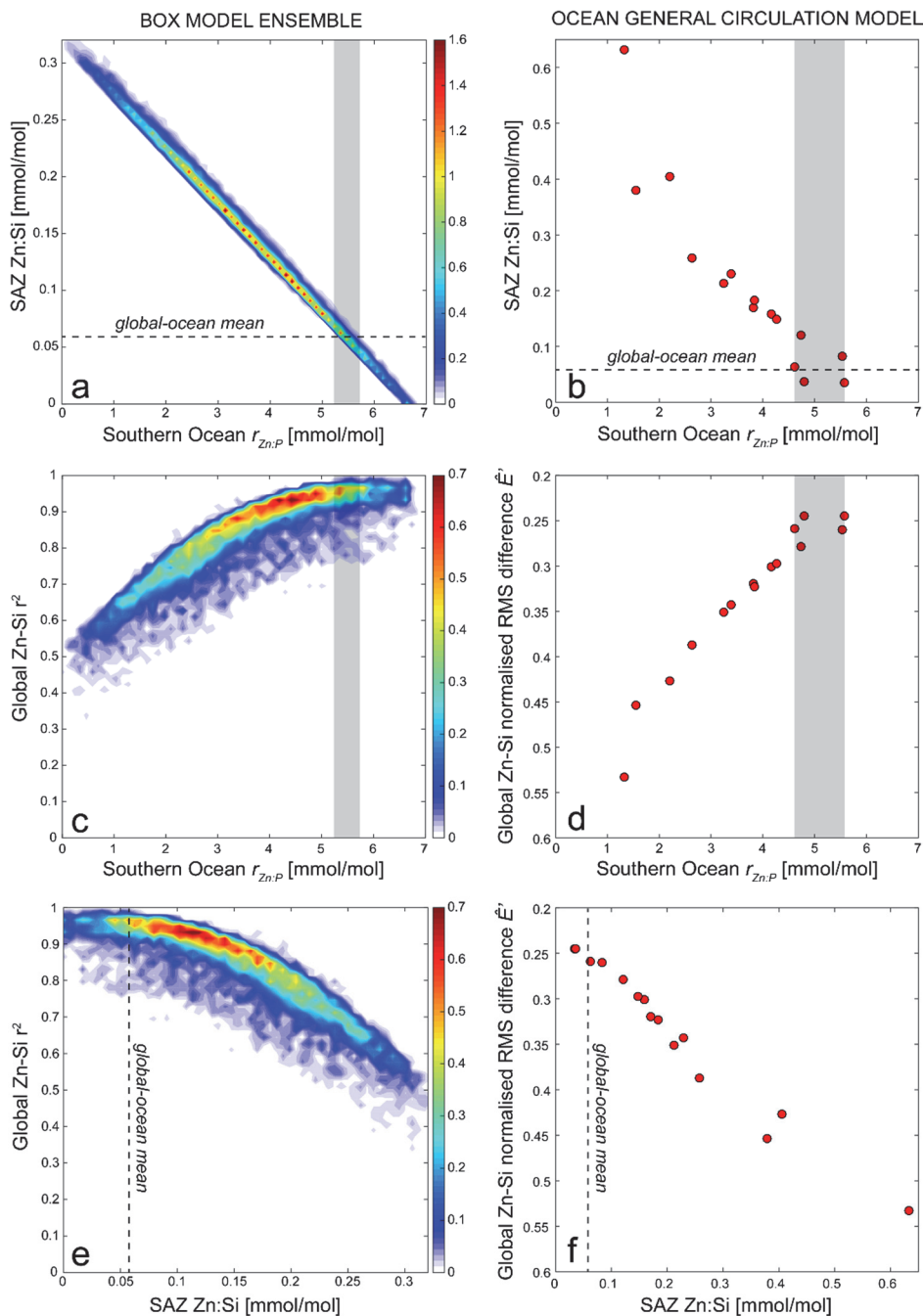
Fig. 8: Systematics of relative Zn and PO₄ drawdown produced by the parameter choices for Eqn. 1 in the OGCM sensitivity simulations. Panels *a* and *c* show the residual Zn as a function of residual PO₄, whilst panels *b* and *d* show the $r_{Zn:P}$ uptake ratios that lead to this relationship. Red circles represent observations in the surface Southern Ocean along the prime meridian by Zhao et al. (2014), normalised to the maximum concentrations of Zn and PO₄ observed along the section (3.7 nM and 1.85 μM respectively) at the Antarctic Divergence. These values were also used as the initial conditions for the calculation of Zn drawdown using Eqn. 1. The vertical blue bar at a residual PO₄ fraction of 40%, the value observed in the SAZ, highlights the range in Zn drawdown produced by the different parameter choices. Note the close correspondence between the degree of drawdown of Zn and model skill at reproducing the global Zn-Si relationship (cf. Fig. 2).
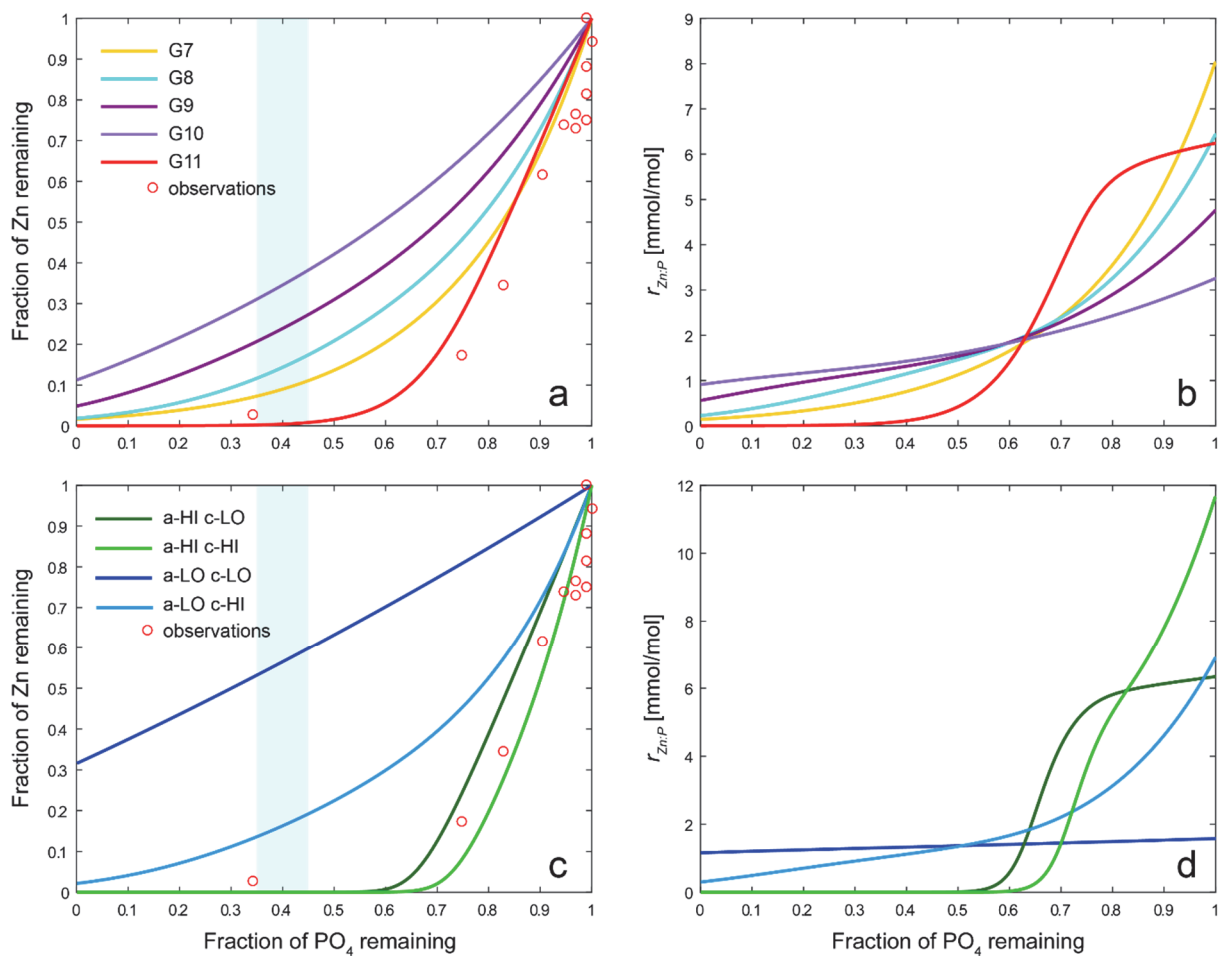
Fig. 9: Cartoon illustrating a potential mechanism for Subantarctic control of global marine elemental correlations. If element *Y* is more strongly depleted than element *X* in the Subantarctic Zone relative to their mean-ocean ratio, the low-concentration endmember subducted into the interior from the Subantarctic will lie below the line connecting the deep ocean and the origin (orange diamond). Circulation and mixing of these upper-ocean water masses will produce the concave-upward relationship seen e.g. between Zn and PO_4 in the global ocean (dashed lines). The blue diamond represents the case in which both elements are present in approximately their global-ocean mean ratio in upper-ocean waters subducted from the Subantarctic, leading to a close-to-linear relationship at the global scale, as for Zn and Si.
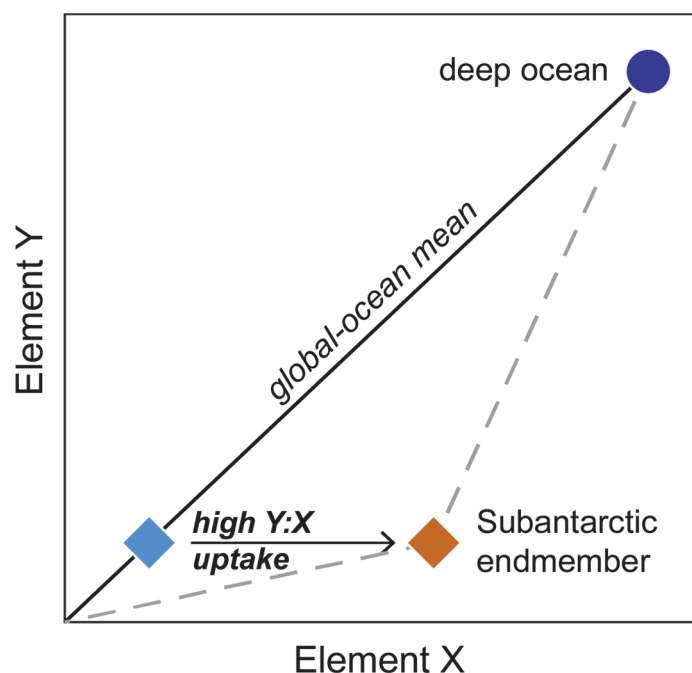
Table 1: Parameter values in OGCM simulations. See Supplementary Information for more details.

Simu-lation	Model variant	Description	Key parameter values m_{Zn} [mol:mol/μM]			$\hat{E}'$ vs. Si	vs. PO$_4$
G1	LIN	0.25× standard slope	0.339			0.53	0.16
G2	LIN	0.5 standard slope	0.679			0.43	0.37
G3	LIN	Standard slope (~*T. oceanica*)	1.357			0.34	0.59
G4	LIN	1.5× standard slope	2.036			0.30	0.70
G5	LIN	2× standard slope	2.714			0.27	0.77
G6	LIN	3× standard slope	4.071			0.26	0.86
			a_{Zn} [mol:mol]	b_{Zn} [μM]	c_{Zn} [mol:mol/μM]		
G7	NONLIN	Eqn. 1 fit to *E. huxleyi A1383*	$2.4×10^{-3}$	$4.0×10^{-5}$	4.7	0.30	0.71
G8	NONLIN	Eqn. 1 fit to *T. weissflogii*	$1.6×10^{-3}$	$1.7×10^{-5}$	4.0	0.32	0.66
G9	NONLIN	Eqn. 1 fit to *T. oceanica*	$1.25×10^{-3}$	$1.0×10^{-5}$	2.9	0.35	0.6
G10	NONLIN	Eqn. 1 fit to *T. pseudonana*	$1.2×10^{-3}$	$8.0×10^{-6}$	1.7	0.39	0.52
G11	NONLIN	Eqn. 1 fit to *E. huxleyi BT6*	$6.0×10^{-3}$	$3.0×10^{-5}$	0.32	0.26	0.81
G12	NONLIN	*aLO*	*$1.2×10^{-3}$*	$1.0×10^{-5}$	2.9	0.35	0.59
G13	NONLIN	*aMID*	*$2.4×10^{-3}$*	$1.0×10^{-5}$	2.9	0.30	0.71
G14	NONLIN	*aHI*	*$6.0×10^{-3}$*	$1.0×10^{-5}$	2.9	0.24	0.90
G15	NONLIN	*bLO*	$1.25×10^{-3}$	*$8.0×10^{-6}$*	2.9	0.35	0.61
G16	NONLIN	*bMID*	$1.25×10^{-3}$	*$3.0×10^{-5}$*	2.9	0.35	0.57
G17	NONLIN	*bHI*	$1.25×10^{-3}$	*$4.0×10^{-5}$*	2.9	0.35	0.56
G18	NONLIN	*cLO*	$1.25×10^{-3}$	$1.0×10^{-5}$	*0.32*	0.45	0.36
G19	NONLIN	*cMID*	$1.25×10^{-3}$	$1.0×10^{-5}$	*1.7*	0.39	0.53
G20	NONLIN	*cHI*	$1.25×10^{-3}$	$1.0×10^{-5}$	*4.7*	0.32	0.67
G21	NONLIN	*aLO-cLO*	$1.2×10^{-3}$	$1.0×10^{-5}$	0.32	0.45	0.34
G22	NONLIN	*aHI-cLO*	$6.0×10^{-3}$	$1.0×10^{-5}$	0.32	0.25	0.85
G23	NONLIN	*aLO-cHI*	$1.2×10^{-3}$	$1.0×10^{-5}$	4.7	0.32	0.66
G24	NONLIN	*aHI-cHI*	$6.0×10^{-3}$	$1.0×10^{-5}$	4.7	0.25	0.92

689 $\hat{E}'$ is the normalised centred root-mean-square difference between the volume-weighted Zn field and the simulated
690 reference field (Si or PO$_4$). It is defined as $\hat{E}' = E'/\sigma_r$, where σ_r is the volume-weighted standard deviation of the
691 reference field and $E' = \left\{ \sum \frac{V_n}{V_{tot}} [(f_n - \bar{f}) - (r_n - \bar{r})]^2 \right\}^{1/2}$, where f represents the Zn field, r the reference field,
692 V_n is the volume of the model cell with Zn concentration f_n, V_{tot} is total volume, and the overbar represents the
693 volume-weighted mean (cf. Taylor, 2001).
694